*American Mineralogist, Volume 101, pages 1360–1372, 2016*

**SPINELS RENAISSANCE: THE PAST, PRESENT, AND FUTURE OF THOSE UBIQUITOUS MINERALS AND MATERIALS**

# Compositional effects on the solubility of minor and trace elements in oxide spinel minerals: Insights from crystal-crystal partition coefficients in chromite exsolution

**Vanessa Colás[1,2,*], José Alberto Padrón-Navarta[3], José María González-Jiménez[4], William L. Griffin[5], Isabel Fanlo[2], Suzanne Y. O'Reilly[5], Fernando Gervilla[6], Joaquín A. Proenza[7], Norman J. Pearson[5], and Monica P. Escayola[8]**

[1]Instituto de Geología, Universidad Nacional Autónoma de México, Ciudad Universitaria, 04510 Ciudad de México, México
[2]Universidad de Zaragoza, Departamento de Ciencias de la Tierra, Pedro Cerbuna 12, 50009 Zaragoza, Spain
[3]Géosciences Montpellier, CNRS and University of Montpellier (UMR5243), 34095 Montpellier, France
[4]Department of Geology and Andean Geothermal Center of Excellence (CEGA), Universidad de Chile, Plaza Ercilla no. 803, Santiago, Chile
[5]ARC Centre of Excellence for Core to Crust Fluid Systems (CCFS) and GEMOC National Key Centre, Department of Earth and Planetary Sciences, Macquarie University, Sydney, New South Wales 2109, Australia
[6]Departamento de Mineralogía y Petrología and Instituto Andaluz de Ciencias de la Tierra (Universidad de Granada-CSIC), Facultad de Ciencias, Avda. Fuentenueva s/n, 18002 Granada, Spain
[7]Departament de Cristal·lografia, Mineralogia i Dipòsits Minerals, Facultat de Geologia, Universitat de Barcelona, Martí i Franquès s/n, 08028 Barcelona, Spain
[8]IDEAN-CONICET, Departamento de Ciencias Geológicas, Facultad de Ciencias Exactas y Naturales, Universidad de Buenos Aires, Intendente Güiraldes 2160, Ciudad Universitaria, Pabellón II-1° EP, Office 29, (1428), Buenos Aires, Argentina

## Abstract

Chromite from Los Congos and Los Guanacos in the Eastern Pampean Ranges of Córdoba (Argentinian Central Andes) shows homogenous and exsolution textures. The composition of the exsolved phases in chromite approaches the end-members of spinel ($MgAl_2O_4$; Spl) and magnetite ($Fe^{2+}Fe^{3+}_2O_4$; Mag) that define the corners of the spinel prism at relatively constant $Cr^{3+}/R^{3+}$ ratio (where $R^{3+}$ is $Cr+Al+Fe^{3+}$). The exsolution of these phases from the original chromite is estimated to have accounted at ≥600 °C on the basis of the major element compositions of chromite with homogenous and exsolution textures that are in equilibrium with forsterite-rich olivine ($Fo_{95}$). The relatively large size of the exsolved phases in chromite (up to ca. 200 μm) provided, for the first time, the ability to conduct in situ analysis with laser ablation-inductively coupled plasma-mass spectrometry for a suite of minor and trace elements to constrain their crystal-crystal partition coefficient between the spinel-rich and magnetite-rich phases ($D_i^{Spl/Mag}$). Minor and trace elements listed in increasing order of compatibility with the spinel-rich phase are Ti, Sc, Ni, V, Ge, Mn, Cu, Sn, Co, Ga, and Zn. $D_i^{Spl/Mag}$ values span more than an order of magnitude, from $D_{Ti}^{Spl/Mag} = 0.30 \pm 0.06$ to $D_{Zn}^{Spl/Mag} = 5.48 \pm 0.63$. Our results are in remarkable agreement with data available for exsolutions of spinel-rich and magnetite-rich phases in other chromite from nature, despite their different $Cr^{3+}/R^{3+}$ ratio. The estimated crystal-crystal partitioning coefficients reflect the effect that crystal-chemistry of the exsolved phases from chromite imposes on all investigated elements, excepting Cu and Sc (and only slightly for Mn). The observed preferential partitioning of Ti and Sc into the magnetite-rich phase is consistent with high-temperature chromite/melt experiments and suggests a significant dependence on $Fe^{3+}$ substitution in the spinel structure. A compositional effect of major elements on Ga, Co, and Zn is observed in the exsolved phases from chromite but not in the experiments; this might be due to crystal-chemistry differences along the $MgFe_{-1}$-$Al_2Fe^{3+}_{-2}$ exchange vector, which is poorly covered experimentally. This inference is supported by the strong covariance of Ga, Co, and Zn observed only in chromite from layered intrusions where this exchange vector is important. A systematic increase of Zn and Co coupled with a net decrease in Ga during hydrous metamorphism of chromitite bodies cannot be explained exclusively by compositional changes of major elements in the chromite (which are enriched in the magnetite component). The most likely explanation is that the contents of minor and trace elements in chromite from metamorphosed chromitites are controlled by interactions with metamorphic fluids involved in the formation of chlorite.

**Keywords:** Chromite exsolution, spinel-magnetite, partition coefficient, minor and trace elements, hydrous metamorphism

---

* E-mail: vcolas86@gmail.com
Special collection papers can be found online at http://www.minsocam.org/MSA/AmMin/special-collections.html.

0003-004X/16/0006–1360$05.00/DOI: http://dx.doi.org/10.2138/am-2016-5611

## INTRODUCTION

A large body of experimental results show that the partitioning of certain minor and trace elements between chromite and melt (±olivine) is sensitive to oxygen fugacity, temperature (Horn et al. 1994; Nielsen et al. 1994; Nielsen and Beard 2000; Canil 1999, 2002; Connolly and Burnett 2003; Righter et al. 2004, 2006; Wijbrans et al. 2015), and, to a lesser extent, to pressure (Canil 1999, 2002; Mallmann and O'Neill 2009). The effect of composition of major and minor elements in chromite has also been experimentally investigated, although less systematically (Horn et al. 1994; Nielsen et al. 1994; Nielsen and Beard 2000; Righter et al. 2006; Mallmann and O'Neill 2009; Wijbrans et al. 2015). These findings have been used to estimate the oxygen fugacity of the mantle source (Lee et al. 2003, 2005; Mallmann and O'Neill 2009), and more generally the petrogenesis of chromite-bearing rocks (Paktunc and Cabri 1995; Barnes 1998; Barnes and Roeder 2001; Kamenetsky et al. 2001; Mondal et al. 2006; Righter et al. 2006; Li et al. 2008; Pagé and Barnes 2009; Dare et al. 2009; González-Jiménez et al. 2011, 2015; Perinelli et al. 2014; Zhou et al. 2014).

Several works have suggested that subsolidus modifications such as fluid-rock interactions can significantly disturb magmatic signatures in chromite (e.g., Evans and Frost 1975; Burkhard 1993; Barnes 2000; Barnes and Roeder 2001; Mukherjee et al. 2010; Gervilla et al. 2012; Prabhakar and Bhattacharya 2013; Singh and Singh 2013; Gargiulo et al. 2013) including their pattern of minor and trace element abundances (Colás et al. 2014; González-Jiménez et al. 2015; Mukherjee et al. 2015). Fluid-rock interactions below 600–650 °C result in (1) the crystallization of hydrous phases such as chlorite and antigorite, (2) the enrichment of chromium and ferric iron in the chromite and, eventually, (3) a coeval change in apparent oxygen fugacity (e.g., Evans and Frost 1975; Candia and Gaspar 1997; Barnes 2000; Barnes and Roeder 2001; Gervilla et al. 2012). It is therefore challenging to unravel as to that ultimately contributes to the disturbance of magmatic signatures in chromite. This hampers the interpretation of the complex behavior of minor and trace elements observed in chromite from metamorphosed chromitites (e.g., Colás et al. 2014; González-Jiménez et al. 2015) or the evaluation of other possible factors such open-system behavior (i.e., element solubility in the fluid phase) that usually predominate during metamorphism of chromite-bearing rocks (e.g., Barnes 2000; Mukherjee et al. 2015).

To date, experimental investigations (at relevant conditions) of hydrous metamorphism in which chromite became modified both texturally and compositionally are lacking. Therefore the evaluation of the compositional factors controlling the solubility of minor and trace elements in these settings relies on explorations from high-temperature experiments, which may suffer additional complications such as bulk element loss (particularly important for Zn; Wijbrans et al. 2015). An alternative approach to investigating the effect of composition, which has not been explored so far, is to use crystal-crystal element partitioning data from exsolved phases in chromite. Exsolution is a process in which chromite solid solution becomes metaestable below critical temperature, and the initial homogeneous chromite separates into at least two different phases that are in equilibrium with each other. Thus, the effect of the major element composition in chromite will be reflected in those minor and trace elements with a crystal-crystal partition coefficient from exsolved phases that is significantly different from unity. Pairs of exsolved phases, with contrasting major element compositions, are relatively common and are developed during post-magmatic cooling (Purvis et al. 1972; Muir and Naldrett 1973; Zakrzewski 1989; Jan et al. 1992; van der Veen and Maaskant 1995; Appel et al. 2002; Garuti et al. 2003; Tamura and Arai 2004, 2005; Krause et al. 2007; Ahmed et al. 2008) and/or high- to medium-grade metamorphism (Loferski and Lipin 1983; Eales et al. 1988; Candia and Gaspar 1997; Abzalov 1998; Proenza et al. 2008). The advantage of this approach is that the temperature (and potentially the oxygen fugacity) of exsolution can be reasonably constrained from the available experimental and thermodynamic data (Turnock and Eugster 1962; Cremer 1969; Muan 1975; Sack and Ghiorso 1991). However, the limitation of this approach for minor and trace elements is directly related with the size of the exsolved phases relative to the spatial resolution of modern laser ablation-inductively coupled plasma-mass spectrometry (LA-ICP-MS).

In this work we report an exceptional case where the size of the exsolved phases in chromite are large enough to be measured in situ with precision minor and trace elements using laser ablation instruments. Thus, we provide the first assessment of the compositional effect on the solubility of minor and some trace elements in natural chromite, specifically along the $\text{MgFe}_{-1}\text{Al}_2\text{Fe}^{3+}_{-2}$ exchange vector (spinel-magnetite join) in the spinel prism. Note that the name "chromite" is used in this work as a general term for Cr-spinel [$(\text{Mg,Fe}^{2+})(\text{Cr,Al,Fe}^{3+})_2\text{O}_4$] from mafic and ultramafic rocks, rather than the sensu stricto definition of chromite as the $\text{Fe}^{2+}$-Cr-rich spinel end-member ($\text{Fe}^{2+}\text{Cr}_2\text{O}_4$; Chr).

## SAMPLES AND METHODS

The samples analyzed in this study were collected from outcrops of six ophiolitic chromitite bodies from the metamorphosed ultramafic massifs of Los Congos and Los Guanacos in the southern part of the Eastern Pampean Ranges

**TABLE 1.** Characterization of the chromitite samples from Los Congos and Los Guanacos ultramafic massifs (Argentina) investigated in this study

| Chromite type | Locality | Sample | Chromitite body | | Exsolved phase | Exsolved phase |
|---|---|---|---|---|---|---|
| | | | Texture | Silicate matrix | composition | proportions[a] |
| Type I | Los Congos | M-25 | Massive | Atg (10 vol%) Cpx (10 vol%) | Chromite-rich | 100% |
| | Los Guanacos | M-17 | | Atg (15 vol%) Cpx (3 vol%) Clc (2 vol%) | | |
| | | 3317 | Semi-massive | Atg (35 vol%) Cpx (4 vol%) Clc (4 vol%) | | |
| | | 2260a | Disseminated | Atg (55 vol%) Cpx (7 vol%) Clc (5 vol%) | | |
| Type II | Los Congos | M-27 | Disseminated | Atg (50–70 vol% ) | Spinel-rich | na[b] |
| | | | | | Magnetite-rich | na |
| Type III | Los Guanacos | 2226 | Massive | Atg (<20 vol%) | Spinel-rich | 39.73% |
| | | | | | Magnetite-rich | 60.27% |
| | | | | | Chromite-rich | 100% |

*Note:* Mineral abbreviations after Whitney and Evans (2010), where antigorite is Atg, clinochlore is Clc, and clinopyroxene is Cpx.

[a] Calculated proportion of each phase in exsolved chromite grains using BSE images on the software Image_J (Rasband 2007). [b] Not available (na).

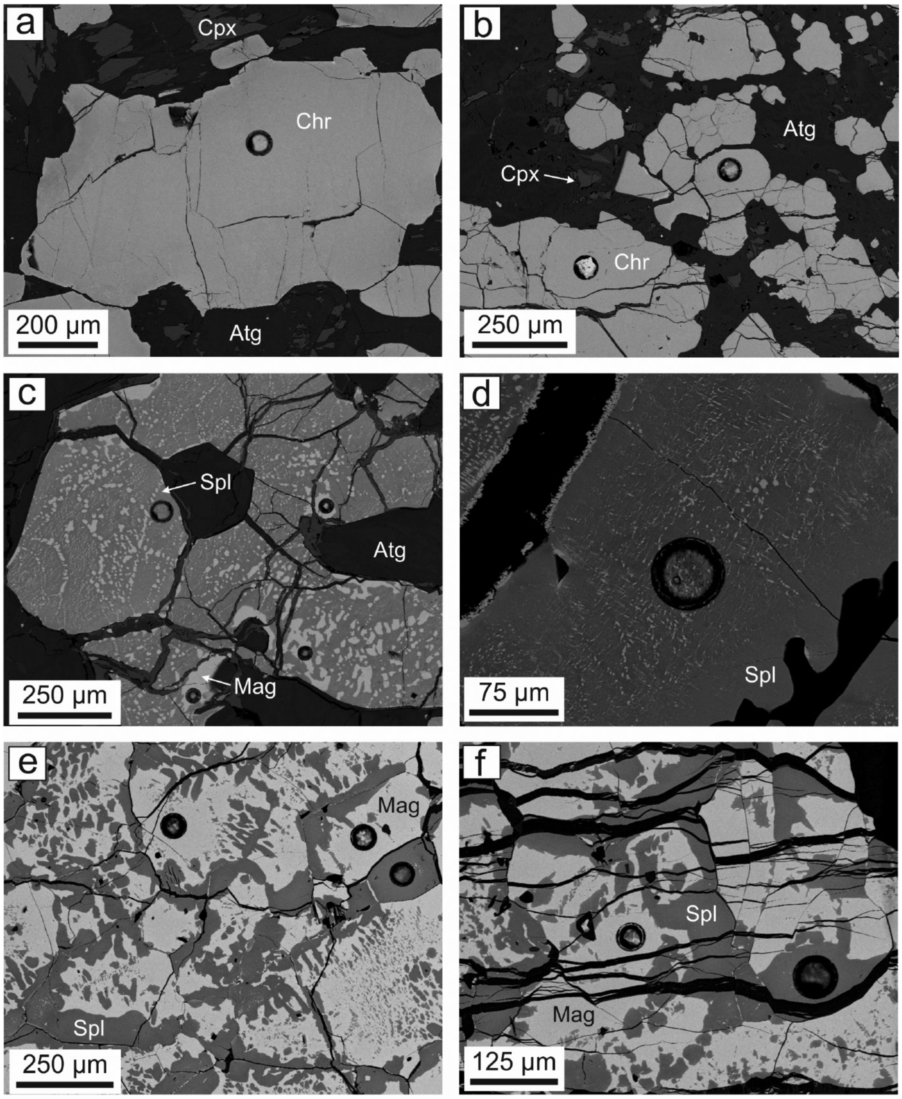

**FIGURE 1.** Backscattered electron (BSE) images of the different textures of chromite identified in the studied chromitites. Type I chromite from Los Congos (**a**) and Los Guanacos (**b**) with relics of clinopyroxene; Type II chromite from Los Congos (**c** and **d**) and Type III chromite from Los Guanacos (**e** and **f**). Mineral abbreviations after Whitney and Evans (2010), where antigorite is Atg, chromite is Chr, clinopyroxene is Cpx, magnetite is Mag, and spinel is Spl.

of Córdoba (Argentinian Central Andes; Proenza et al. 2008). These two massifs are separated by 6 km and mainly consist of highly serpentinized metaharzburgite that enclose bodies of metadunites and metalherzolites and sills of metagabbro. The location and detailed geological description of the studied ultramafic massifs have been given elsewhere (Proenza et al. 2008; Escayola et al. 2004). Escayola et al. (2004) suggested that these metaultramafic rocks where subjected to four metamorphic events, including: (1) low-grade sea-floor metamorphism, overprinted by (2) granulite-facies metamorphism (7.3–9.4 kbar and 760–860 °C; Rapela et al. 1998; Martino et al. 2010), (3) retrograde amphibolite-facies metamorphism (3.5–7.3 kbar and 590–730 °C; Rapela et al. 1998; Martino et al. 2010) and (4) a low-temperature hydrothermal event.

The chromitite bodies show massive (>85 vol% chromite), semi-massive (60–85 vol% chromite) and disseminated (<60 vol% chromite) textures (Table 1). Chromite grains are predominantly subhedral and less frequently anhedral with rounded shapes, and have a fracture network of variable density (Fig. 1). Silicate minerals in the chromitites are mainly antigorite, clinochlore, and occasionally clinopyroxene (Fig. 1; Table 1). These minerals are also included in chromite grains. The primary olivine is not preserved (Proenza et al. 2008), whereas the fractures that usually cut across chromite grains are filled with serpentinite, chlorite, and less frequently carbonates.

The careful study of chromite using transmitted and reflected optical microscopy and scanning electron microscope (JEOL SM 6400 SEM belonging to University of Zaragoza, Spain) reveals the presence of three textural varieties of chromite (Fig. 1; Table 1).

Type I chromite is optically and compositionally homogeneous and occurs in clinopyroxene-bearing massive, semi-massive, and disseminated chromitites from Los Congos and Los Guanacos (Figs. 1a–1b; Table 1).

Type II chromite shows an inhomogeneous (exsolved) texture and occurs in clinopyroxene-free massive, semi-massive, and disseminated chromitite samples from Los Congos, but the disseminated chromitite sample was selected in this study. It is composed of a low-reflective phase that is complexly intergrown with a high-reflective phase (Figs. 1c–1d; Table 1). The high-reflective phase occurs as coarse, sub-rounded, irregular, and lobated blebs (from 5–10 to 150 μm) that are distributed randomly throughout the grains, concentrated in the rims or forming linear strings (Fig. 1c). The low-reflective phase itself contains another set of exsolved high-reflective phases forming very fine lamellae (ca. 1 μm thick), which are arranged in dense networks with an apparent crystallographic control (Fig. 1d).

Type III chromite is restricted to clinopyroxene-free massive chromitite samples from Los Congos and Los Guanacos, however only chromitite sample from Los Guanacos were studied (Table 1). This chromite shows an irregular coarse mottling or symplectic texture composed of variable proportions of high-reflective and low-reflective phases (Figs. 1e–1f). The exsolved phases in Type III chromites are coarser (up to ca. 200 μm) than in the Type II ones (below ca. 40 μm) (Figs. 1c–1f).

The contents of major and minor elements in the different phases of these three types of chromite were determined quantitatively using both microprobe and LA-ICP-MS at the Geochemical Analysis Unit at CCFS/GEMOC, Macquarie University, Sydney (Australia). Electron-microprobe analyses (EMPA) were obtained by wavelength-dispersive spectrometer (WDS mode) with a Cameca SX-100 under the following working conditions: 20 kV acceleration voltage, 20 nA beam current, and 2–3 μm beam size. Peak counting times were 10 s for Cr, Fe, Ti, V, Mn, Zn, and Ni; 20 s for Mg; and 30 s for Al. Standards used were a combination of natural and synthetic minerals and pure metals. Structural formulas of chromite were calculated assuming stoichiometry, following the procedure of Droop (1987).

LA-ICP-MS analyses were carried out using a New Wave UP 266 laser ablation unit coupled to an Agilent 7500cs ICP-MS. The chromite was analyzed for the following masses: $^{45}$Sc, $^{47}$Ti, $^{51}$V, $^{55}$Mn, $^{59}$Co, $^{60}$Ni, $^{65}$Cu, $^{66}$Zn, $^{71}$Ga, $^{72}$Ge, and $^{118}$Sn. The isotopes $^{29}$Si and $^{42}$Ca were monitored to control the presence of silicate inclusions. The analyses were conducted using a 30–50 μm beam diameter, 5 Hz frequency, and 0.152 mJ/pulse power, during 180 s analysis (60 s for the gas blank and 120 s on the chromite). The smallest beam diameters (~30 μm) were used during the measurement of the small blebs in Type II chromite. The GLITTER software (Griffin et al. 2008) was used for data reduction. Count signal vs. time diagrams were checked during single ablation runs to avoid the ablation of mixtures of low-reflective and high-reflective phases in chromite with exsolution textures (Supplementary Fig. 1[1]). The analyses were calibrated against the NIST 610 silicate glass (National Institute Standards and Technology, Gaithersburg, U.S.A.) (Norman et al. 1996). Aluminum values obtained by EPMA were used as internal standard. The basaltic glass BCR-2g (Norman et al. 1998; Gao et al. 2002) and the in-house secondary chromite standard LCR-1 (Lace mine, South Africa; Locmelis et al. 2011) were analyzed as unknowns during each analytical run to check the accuracy and precision of the analyses. The results obtained during the analyses of these two standards display very good reproducibility (0.4–11.4%) (Supplementary Table 1[1]).

## RESULTS

### Major element composition

The composition of Type I chromite in massive chromitites from Los Congos and Los Guanacos follows a distinctive linear trend defined by an increase of Cr# [Cr/(Cr+Al) in atomic ratio] from 0.47 to 0.72 coeval with a decrease of Mg# [Mg/(Mg+Fe$^{2+}$) in atomic ratio] from 0.68 to 0.52 (Fig. 2a; Table 2). In Los Guanacos the Type I chromite from semi-massive and disseminated chromitites show similar trends but are displaced toward lower Mg# (0.48–0.55 in semi-massive chromitites; 0.42–0.52 in disseminated chromitites) (Fig. 2a; Table 2). The ratio of Fe$^{3+}$ to other trivalent cations [Fe$^{3+}$/R$^{3+}$ = Fe$^{3+}$/(Fe$^{3+}$+Al+Cr) in atomic ratio] increases from semi-massive (Fe$^{3+}$/R$^{3+}$ = 0.08–0.10) to disseminated chromitites (Fe$^{3+}$/R$^{3+}$ = 0.18–0.26) (Fig. 2b; Table 2). It is noteworthy that the massive chromitites show Fe$^{3+}$/R$^{3+}$ ratio (0.13–0.21) intermediate between these two extremes (Fig. 2b; Table 2). All textural types are poor in TiO$_2$, consistent with the absence of ilmenite exsolution in chromite.

The original composition of Type III chromite from Los Guanacos, prior to exsolution, was estimated in individual grains based on EPMA analyses (Table 2) and the areal proportion of the exsolved phases in BSE images, using the Image-J software (Rasband 2007) (Table 1). The composition prior to exsolution of Type II chromite from Los Congos could not be integrated due to the fine networks of lamellae in the low-reflective domains (cf. Fig. 1d). The estimated original composition of Type III chromite has Cr# (0.55–0.60) and Mg# (0.42–0.49) similar to Type I chromite from disseminated chromitite (Cr# = 0.55–0.63 and Mg# = 0.42–0.52) (Figs. 2a and 2c; Table 2), but it shows the lowest Cr$^{3+}$/R$^{3+}$ ratio [Cr$^{3+}$/(Cr$^{3+}$+Fe$^{3+}$+Al) in atomic ratio] (≈ 0.34) and the highest Fe$^{3+}$/R$^{3+}$ ratio (0.40–0.44) among all textural groups (Figs. 2b and 2d; Table 2).

The low-reflective phase in Type II and Type III chromite is rich in spinel ss (Spl; MgAl$_2$O$_4$), with higher Mg# (0.56–0.63 in Type II chromite and 0.64–0.73 in Type III chromite) but lower Cr# (0.50–0.54 in Type II chromite and 0.41–0.43 in Type III chromite) than the high-reflective phase (Mg# = 0.21–0.23 and Cr# = 0.85–0.87 in Type II chromite; Mg# = 0.29–0.33 and Cr# = 0.76–0.79 in Type III chromite), which is rich in magnetite (Mag; Fe$^{2+}$Fe$^{3+}_2$O$_4$) (Fig. 2c; Table 2). This is depicted in the spinel prism (Fig. 2d), which shows that the exsolved phases plot along a compositional field between the spinel (Fe$^{3+}$/R$^{3+}$ = 0.12–0.21) and magnetite (Fe$^{3+}$/R$^{3+}$ = 0.55–0.65) corners (i.e., along the MgFe$_{-1}$-Al$_2$Fe$^{3+}_{-2}$ exchange vector) (Table 2). In contrast to other exsolved phases in chromite from the literature (e.g., Loferski and Lipin 1983; Tamura and Arai 2004, 2005) the Cr$^{3+}$/R$^{3+}$ ratio in the exsolutions of spinel-rich and magnetite-rich phases from Type II and Type III chromite is constant (from 0.29 to 0.43 and from 0.30 to 0.37, respectively) (Fig. 2d; Table 2).

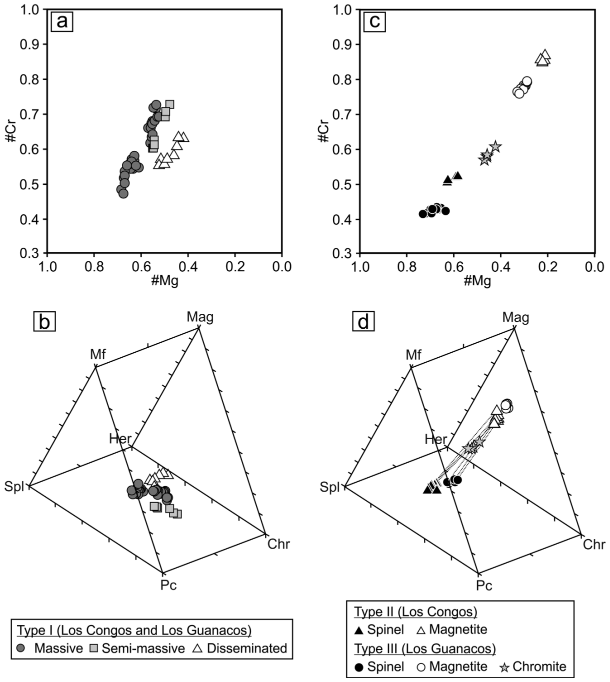

**FIGURE 2.** Compositional variations of the different textures of chromite from the studied chromitites in terms of Mg# [Mg/(Mg+Fe$^{2+}$) atomic ratio] vs. Cr# [Cr/(Cr+Al) atomic ratio] and the spinel prism. Legend provided as inset in the figure and Matlab script to plot spinel prism in 3D is provided in the Appendix.

---

[1] Deposit item AM-16-65611, Supplemental Table and Figure. Deposit items are free to all readers and found on the MSA web site, via the specific issue's Table of Contents (go to http://www.minsocam.org/MSA/AmMin/TOC/).

**TABLE 2.** Average composition of major, minor, and trace elements in chromite grains from Los Congos and Los Guanacos ultramafic massifs (Argentina) analyzed by EMPA and LA-ICP-MS

| Chromite type | Type I | | | | Type II | | Type III | | |
|---|---|---|---|---|---|---|---|---|---|
| Location | Los Congos | | Los Guanacos | | Los Congos | | Los Guanacos | | |
| Texture | Massive | | Semi-massive | Disseminated | Disseminated | | Massive | | |
| Sample | M-25 | M-17 | 3317 | 2260a | M-27 | | 2226 | | |
| | | | | | Spinel-rich | Magnetite-rich | Spinel-rich | Magnetite-rich | Chromite-rich[a] |
| | n = 17 | n = 16 | n = 7 | n = 8 | n = 6 | n = 5 | n = 10 | n = 9 | n = 19 |
| TiO$_2$ (wt%)[b] | 0.19 ± 0.05 | 0.14 ± 0.02 | 0.19 ± 0.05 | 0.19 ± 0.03 | 0.8 ± 0.83 | 0.62 ± 0.07 | 0.05 ± 0.02 | 0.25 ± 0.01 | 0.17 |
| Al$_2$O$_3$ | 21.4 ± 2.07 | 14.16 ± 1.55 | 17.13 ± 3.04 | 17.07 ± 2.08 | 21.02 ± 1.25 | 2.41 ± 0.11 | 28.00 ± 1.14 | 4.50 ± 0.44 | 13.83 |
| Cr$_2$O$_3$ | 36.79 ± 1.30 | 42.93 ± 2.00 | 47.58 ± 2.89 | 35.92 ± 1.01 | 33.23 ± 0.74 | 21.12 ± 0.76 | 30.63 ± 0.56 | 23.36 ± 0.87 | 26.24 |
| Fe$_2$O$_3$[c] | 14.65 ± 1.85 | 15.75 ± 0.89 | 7.03 ± 0.42 | 18.68 ± 2.08 | 16.8 ± 0.39 | 46.28 ± 0.76 | 14.50 ± 1.69 | 43.90 ± 1.41 | 32.22 |
| FeO | 13.63 ± 0.75 | 16.37 ± 0.33 | 17.99 ± 0.83 | 19.66 ± 1.12 | 15.71 ± 1.24 | 25.27 ± 0.22 | 12.56 ± 1.06 | 23.00 ± 0.40 | 18.86 |
| V$_2$O$_3$ | 0.12 ± 0.02 | 0.13 ± 0.01 | 0.19 ± 0.03 | 0.07 ± 0.02 | 0.19 ± 0.02 | 0.36 ± 0.02 | 0.07 ± 0.03 | 0.19 ± 0.01 | 0.14 |
| MnO | 0.46 ± 0.03 | 1.04 ± 0.06 | 0.40 ± 0.03 | 0.36 ± 0.05 | 0.87 ± 0.08 | 0.9 ± 0.07 | 0.45 ± 0.03 | 0.68 ± 0.05 | 0.59 |
| MgO | 14.18 ± 0.59 | 11.15 ± 0.34 | 11.01 ± 0.85 | 9.93 ± 0.95 | 12.68 ± 0.63 | 3.97 ± 0.15 | 15.32 ± 0.81 | 5.67 ± 0.29 | 9.50 |
| ZnO | 0.09 ± 0.08 | 0.26 ± 0.03 | 0.20 ± 0.04 | 0.12 ± 0.07 | 0.37 ± 0.07 | 0 ± 0.00 | 0.44 ± 0.04 | 0.09 ± 0.09 | 0.23 |
| NiO | 0.2 ± 0.05 | 0.22 ± 0.06 | 0.08 ± 0.07 | 0.18 ± 0.06 | 0.19 ± 0.02 | 0.75 ± 0.02 | 0.20 ± 0.02 | 0.75 ± 0.05 | 0.53 |
| Total | 101.8 ± 0.7 | 102.1 ± 0.4 | 101.8 ± 0.6 | 102.3 ± 0.7 | 101.9 ± 0.79 | 101.7 ± 0.16 | 102.2 ± 0.4 | 102.4 ± 0.4 | 102.3 |
| **Atoms per formula unit calculated on the basis of four oxygen atoms** | | | | | | | | | |
| Al | 0.77 | 0.53 | 0.64 | 0.64 | 0.76 | 0.10 | 0.97 | 0.18 | 0.53 |
| Cr | 0.88 | 1.08 | 1.18 | 0.90 | 0.81 | 0.60 | 0.71 | 0.64 | 0.67 |
| Fe$^{3+}$ | 0.34 | 0.38 | 0.17 | 0.45 | 0.39 | 1.25 | 0.32 | 1.15 | 0.79 |
| V | 0.00 | 0.00 | 0.00 | 0.00 | 0.00 | 0.01 | 0.00 | 0.01 | 0.00 |
| Mg | 0.64 | 0.53 | 0.52 | 0.47 | 0.58 | 0.21 | 0.67 | 0.29 | 0.46 |
| Fe$^{2+}$ | 0.35 | 0.44 | 0.47 | 0.52 | 0.40 | 0.76 | 0.31 | 0.67 | 0.51 |
| Ti | 0.00 | 0.00 | 0.00 | 0.00 | 0.02 | 0.02 | 0.00 | 0.01 | 0.00 |
| Mn | 0.01 | 0.03 | 0.01 | 0.01 | 0.02 | 0.03 | 0.01 | 0.02 | 0.02 |
| Ni | 0.00 | 0.01 | 0.00 | 0.00 | 0.00 | 0.02 | 0.00 | 0.02 | 0.01 |
| Mg#[d] | 0.61–0.68 | 0.52–0.57 | 0.48–0.55 | 0.42–0.52 | 0.56–0.63 | 0.21–0.23 | 0.64–0.73 | 0.29–0.33 | 0.42–0.49 |
| Cr#[e] | 0.47–0.58 | 0.62–0.72 | 0.60–0.73 | 0.55–0.63 | 0.50–0.54 | 0.85–0.87 | 0.41–0.43 | 0.76–0.79 | 0.55–0.60 |
| Cr$^{3+}$/R$^{3+}$[f] | 0.41–0.47 | 0.51–0.60 | 0.55–0.67 | 0.44–0.48 | 0.40–0.43 | 0.29–0.32 | 0.35–0.37 | 0.30–0.34 | 0.34 |
| Fe$^{3+}$/R$^{3+}$[g] | 0.13–0.21 | 0.17–0.20 | 0.08–0.10 | 0.18–0.26 | 0.19–0.21 | 0.63–0.65 | 0.12–0.18 | 0.55–0.62 | 0.40–0.44 |
| | n = 11 | n = 17 | n = 7 | | | | n = 6 | n = 7 | n =13 |
| Sc (ppm) | 1.92 ± 0.97 | 6.00 ± 1.44 | 0.72 ± 0.38 | | | | 1.43 ± 0.40 | 4.10 ± 0.61 | 3.04 |
| Ti | 1159 ± 135 | 835 ± 96 | 1011 ± 252 | | | | 377 ± 94 | 1198 ± 165 | 872 |
| V | 830 ± 70 | 775 ± 58 | 1197 ± 50 | | | | 668 ± 95 | 1135 ± 159 | 950 |
| Mn | 3113 ± 157 | 7457 ± 376 | 2789 ± 259 | | | | 3580 ± 372 | 4455 ± 666 | 4108 |
| Co | 306 ± 10 | 341 ± 14 | 381 ± 9 | | | | 664 ± 33 | 359 ± 41 | 480 |
| Ni | 1710 ± 337 | 1609 ± 315 | 750 ± 80 | | | | 2133 ± 411 | 5106 ± 747 | 3925 |
| Cu | 0.82 ± 0.69 | 2.61 ± 1.87 | 0.12 ± 0.02 | | | | 12.11 ± 3.79 | 14.26 ± 4.09 | 13.41 |
| Zn | 1345 ± 74 | 2526 ± 164 | 2261 ± 201 | | | | 5476 ± 348 | 991 ± 75 | 2773 |
| Ga | 26.49 ± 2.54 | 14.77 ± 2.32 | 24.16 ± 3.49 | | | | 28.28 ± 1.09 | 13.01 ± 1.80 | 19.08 |
| Ge | 2.07 ± 0.31 | 2.48 ± 0.26 | 1.86 ± 0.27 | | | | 2.64 ± 0.48 | 4.01 ± 0.59 | 3.47 |
| Rb | 0.63 ± 0.12 | 1.77 ± 0.45 | 0.91 ± 0.28 | | | | 0.50 ± 0.19 | 0.44 ± 0.05 | 0.46 |
| Sn | 0.80 ± 0.24 | 7.14 ± 0.93 | 1.27 ± 0.21 | | | | 0.95 ± 0.26 | 0.94 ± 0.21 | 0.95 |

[a] Composition of chromite grains prior to exsolution estimated from the average content and proportions (see Table 1) of spinel-rich and magnetite-rich phases. [b] Uncertainties are given as 1σ standard deviation. [c] Fe$_2$O$_3$ contents of chromite were computed assuming R$_3$O$_4$ stoichiometry and charge balance. [d] Range of Mg# [Mg/(Mg+Fe$^{2+}$) atomic ratio]. [e] Range of Cr# [Cr/(Cr+Al) atomic ratio]. [f] Range of Cr$^{3+}$/R$^{3+}$ ratio [Cr/(Fe$^{3+}$+Al+Cr) in atomic ratio]. [g] Range of Fe$^{3+}$/R$^{3+}$ ratio [Fe$^{3+}$/(Fe$^{3+}$+Al+Cr) in atomic ratio].

## Crystal-crystal partition coefficients

Minor and trace element concentrations for Type I and Type III chromite from Los Congos and Los Guanacos are shown in Table 2. Analyses of Type II chromite from Los Congos were excluded from the following treatment because the beam size of LA-ICP-MS (~30–50 μm) is larger than the size of the exsolved phases (cf. Fig. 1d), and also because internal normalization with the EPMA data is not straightforward. Table 3 shows two statistical tests comparing the concentrations of minor and trace elements in the spinel-rich and magnetite-rich phases in Type III chromite. The differences in concentration between the two phases are statistically significant for all elements except for Cu and Sn. These tests also reveal that the difference in Mn is less robust than for the rest of the elements. Assuming that the exsolved phases represent an equilibrium assemblage at a given bulk composition, temperature, pressure, and $f_{O_2}$, a set of spinel-rich/magnetite-rich crystal-crystal partition coefficients can be evaluated from the relative change in concentration of the two exsolved phases. Crystal-crystal empirical partition coefficients are calculated based on the LA-ICP-MS data according to the following expression:

$$D_{\mathrm{i}}^{\mathrm{Spl/Mag}} = \frac{C_{\mathrm{i}}^{\mathrm{Spl}}}{C_{\mathrm{i}}^{\mathrm{Mag}}} \qquad (1)$$

where the spinel-rich/magnetite-rich partition coefficient ($D_{\mathrm{i}}^{\mathrm{Spl/Mag}}$) of an element $i$ is defined as the ratio of the concentration of the element (in parts per million) in the pair of exsolutions of spinel-rich ($C_{\mathrm{i}}^{\mathrm{Spl}}$) and the magnetite-rich ($C_{\mathrm{i}}^{\mathrm{Mag}}$) phases. Given the restricted range in major element composition of the exsolved phases (see above) two approaches can be followed to

**TABLE 3.** Statistics of minor and trace elements of Type III chromite from Los Guanacos ultramafic massif (Argentina)[a]

| | | $^{45}$Sc | $^{47}$Ti | $^{51}$V | $^{55}$Mn | $^{59}$Co | $^{60}$Ni | $^{65}$Cu | $^{66}$Zn | $^{71}$Ga | $^{72}$Ge | $^{118}$Sn |
|---|---|---|---|---|---|---|---|---|---|---|---|---|
| $C_i^{\mathrm{Spl}\,b}$ | Mean | 1.43 | 377 | 668 | 3580 | 664 | 2133 | 12.11 | 5476 | 28.28 | 2.64 | 0.95 |
| (*n* =6) | Median | 1.26 | 331 | 620 | 3444 | 673 | 1977 | 12.49 | 5456 | 28.01 | 2.63 | 1.05 |
| | Std. Error | 0.16 | 38 | 39 | 152 | 14 | 168 | 1.55 | 142 | 0.45 | 0.20 | 0.11 |
| $C_i^{\mathrm{Mag}\,c}$ | Mean | 4.10 | 1198 | 1135 | 4455 | 359 | 5106 | 14.26 | 991 | 13.01 | 4.01 | 0.94 |
| (*n* =7) | Median | 4.17 | 1202 | 1131 | 4481 | 357 | 5172 | 15.38 | 1000 | 13.34 | 4.03 | 0.94 |
| | Std. Error | 0.23 | 63 | 60 | 252 | 16 | 283 | 1.54 | 28 | 0.68 | 0.22 | 0.08 |
| | | | | | **Comparison of means** | | | | | | | |
| T test | *p* | 2.11E-6 | 7.45E-7 | 7.11E-5 | 1.45E-2 | 1.65E-8 | 5.44E-6 | 3.46E-1 | 2.74E-7 | 3.72E-9 | 7.07E-4 | 9.22E-1 |
| | Result | R | R | R | R | R | R | **FR** | R | R | R | **FR** |
| Mann-Witney U test | *p* | 3.41E-3 | 3.41E-3 | 5.34E-3 | 3.83E-2 | 3.41E-3 | 3.41E-3 | 2.84E-1 | 3.41E-3 | 3.41E-3 | 8.22E-3 | 9.43E-1 |
| | Result | R | R | R | R | R | R | **FR** | R | R | R | **FR** |
| | | | | | **Partition coeficients** | | | | | | | |
| $D_i^{\mathrm{Spl/Mag}\,d}$ | Mean | 0.35 | 0.31 | 0.59 | 0.80 | 1.85 | 0.42 | 0.85 | 5.52 | 2.17 | 0.66 | 1.01 |
| | Error[e] | 0.04 | 0.04 | 0.05 | 0.06 | 0.09 | 0.04 | 0.14 | 0.21 | 0.12 | 0.06 | 0.14 |
| $D_i^{\mathrm{Spl/Mag}\,f}$ | Mean | 0.33 | 0.30 | 0.59 | 0.81 | 1.85 | 0.42 | 1.11 | 5.48 | 2.23 | 0.64 | 1.12 |
| | Std. Dev. | 0.09 | 0.06 | 0.11 | 0.15 | 0.23 | 0.09 | 0.57 | 0.63 | 0.40 | 0.12 | 0.70 |

[a] Reported descriptive statistics are the mean, median, and standard errors of "*n*" samples of each phase from Type III chromite of Los Guanacos. Two statistical tests are also reported comparing the minor and trace elements of spinel-rich with those of magnetite-rich: T test = results of the T test for unequal and unknown variances; Mann-Whitney U test = results of the nonparametric (i.e., no assumptions about the distribution of the underlying population) Mann-Whitney U test. In both tests the null hypothesis is the two means are equal, and the level of significance is 5; p is the empirical significance test of a given test such as $p < 0.05$ indicates a confidence level greater than 0.99; R and FR stand for "reject" and "fail to reject" the null hypothesis, respectively. If rejected, it is likely that the two means are different (i.e., two populations) with a confidence level of p. All statistical computations were carried out using statistical tools from OriginPro (version 15) software. [b, c] Content of the element (in ppm) in the spinel-rich ($C_i^{\mathrm{Spl}}$) and the magnetite-rich ($C_i^{\mathrm{Mag}}$) phases. [d] Average of partition coefficient no assuming pairs. [e] Error of $D_i^{\mathrm{Spl/Mag}}$ was calculated using the error propagation furmulae for a division: $\delta D_i^{\mathrm{Spl/Mag}} = D_i^{\mathrm{Spl/Mag}}\sqrt{(\delta C_i^{\mathrm{Spl}}/C_i^{\mathrm{Spl}})^2 + (\delta C_i^{\mathrm{Mag}}/C_i^{\mathrm{Mag}})^2}$, where $\delta C_i^{\mathrm{Spl}}$ and $\delta C_i^{\mathrm{Mag}}$ are the standard error of the content of the element (in ppm) in the spinel-rich and magnetite-rich phases, respectively. [f] Average of partition coefficient for individual pairs.

estimate $D_i^{\mathrm{Spl/Mag}}$: (1) averaging partition coefficient values for individual pairs (five pairs of spatially related phases assumed to have been exsolved from the same grain) and (2) computing partition coefficient values based on the average composition of six spinel-rich and seven magnetite-rich phases (where no assumptions of pairs are made). The two approaches give nearly identical results, however the averaged partition coefficient for individual pairs was used for comparison (Table 3).

**Minor elements.** Ti, Ni, V, Mn, Co, and Zn have been listed in increasing order of compatibility with the spinel-rich phase (Fig. 3; Table 3). Empirical partition coefficients span more than an order of magnitude, from $D_{\mathrm{Ti}}^{\mathrm{Spl/Mag}} = 0.30 \pm 0.06$ to $D_{\mathrm{Zn}}^{\mathrm{Spl/Mag}} = 5.48 \pm 0.63$ (Table 3). Minor elements obtained in this work can be readily compared to EPMA analyses of other exsolved phases in chromite from the literature (Fig. 3; see Appendix for sources), where the exchange vector is systematically along the spinel-magnetite corners and with constant $\mathrm{Cr}^{3+}/\mathrm{R}^{3+}$ ratio for each pair (although variable from pair to pair). All elements are in good agreement except for $D_{\mathrm{V}}^{\mathrm{Spl/Mag}}$, $D_{\mathrm{Co}}^{\mathrm{Spl/Mag}}$, and $D_{\mathrm{Zn}}^{\mathrm{Spl/Mag}}$, which are higher in this study compared to the literature data ($0.59 \pm 0.11$ vs. $0.31 \pm 0.14$ for V; $1.85 \pm 0.23$ vs. $0.92 \pm 0.11$ for Co, and $5.48 \pm 0.63$ vs. $3.32 \pm 1.98$ for Zn, respectively) (Fig. 3). The general agreement is nevertheless remarkable considering that no attempt has been made to subdivide the literature data based on geological setting, temperature or oxygen fugacity conditions and that $\mathrm{Cr}^{3+}/\mathrm{R}^{3+}$ ratio in the literature data spans the whole possible range along the miscibility gap (Sack and Ghiorso 1991).

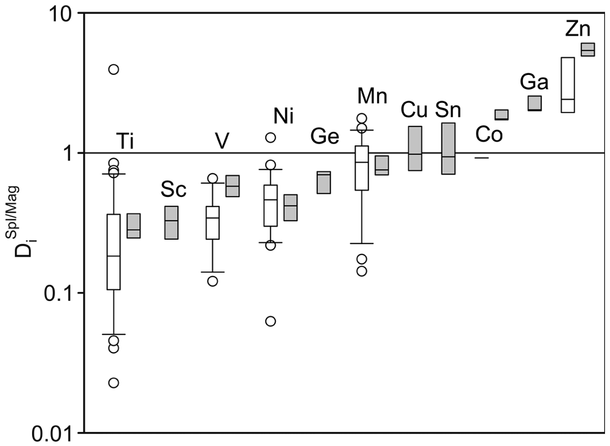

**FIGURE 3.** Box chart diagrams illustrating the statistical crystal-crystal partition coefficient of certain minor and trace elements in exsolved phases within chromite from this study (gray boxes) and from the literature (white boxes). Elements arranged in increasing order of compatibility with the spinel-rich phase. Data sources are listed in the Appendix.

**Trace elements.** Sc, Ge, Cu, Sn, and Ga are listed in increasing order of compatibility with the spinel-rich phase (Table 3), spanning also almost an order of magnitude (from $D_{\mathrm{Sc}}^{\mathrm{Spl/Mag}} = 0.33 \pm 0.09$ to $D_{\mathrm{Ga}}^{\mathrm{Spl/Mag}} = 2.23 \pm 0.40$; Table 3).

## DISCUSSION

### Temperature of the exsolution process

The exsolution of spinel-rich and magnetite-rich phases from a precursor chromite from Los Congos and Los Guanacos seems to be independent of the texture of the chromitite body, but always it is restricted to clinopyroxene-free assemblages (Table 1). It is interesting to note that the observed exsolutions are in chromitite samples where the main silicate is antigorite rather than clinochlore (Table 1). Clinochlore (but not antigorite) is the expected phyllosilicate produced during hydrous metamorphism of chromite-olivine-bearing rocks under amphibolite- to greenschist-facies conditions (e.g., Gervilla et al. 2012). The extensive occurrence of antigorite might indicate an orthopyroxene-bearing chromitite as the original protolith hosting Type II and Type III chromite prior to hydration (e.g., Bach et al. 2006; Frost and Beard 2007). However, it is clear

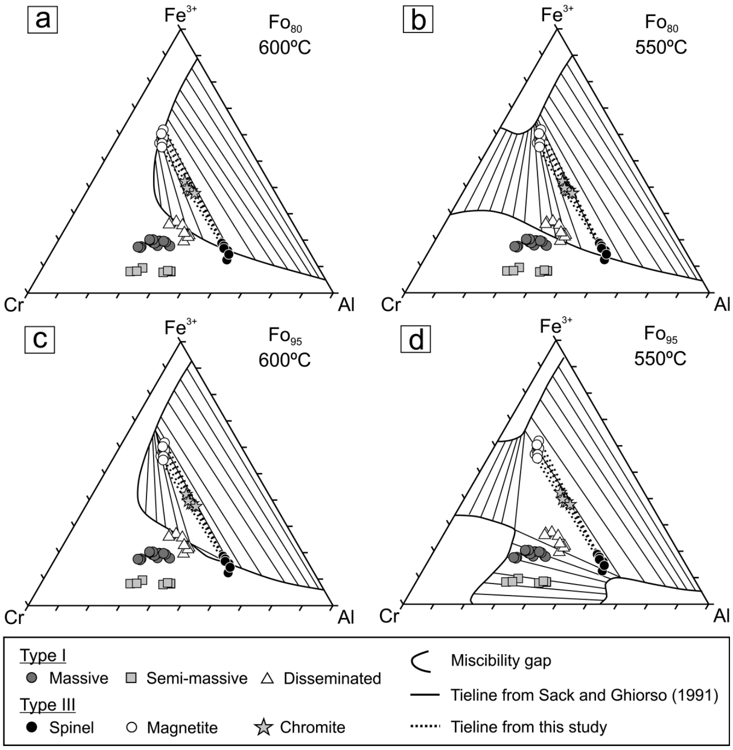

**FIGURE 4.** Isothermal (isobaric) sections determined at 600 and 550 °C through the spinel prism calculated by Sack and Ghiorso (1991) for fixed Fe-Mg potentials defined by $Fo_{80}$ (**a** and **b**) and $Fo_{95}$ (**c** and **d**). Legend provided as inset in the figure.

that the main factor controlling the exsolution was the $Cr^{3+}/R^{3+}$ ratio of the original chromite (Figs. 2 and 4). Only chromite with $Cr^{3+}/R^{3+}$ ratio <0.35 (and concomitant high $Fe^{3+}/R^{3+}$ > 0.40) show exsolutions of spinel-rich and magnetite-rich phases (Table 2). This feature has been observed in all previously reported studies of exsolution in chromite (Purvis et al. 1972; Muir and Naldrett 1973; Loferski and Lipin 1983; Eales et al. 1988; Zakrzewski 1989; Jan et al. 1992; van der Veen and Maaskant 1995; Appel et al. 2002; Garuti et al. 2003; Tamura and Arai 2004, 2005; Krause et al. 2007; Ahmed et al. 2008). The position of the miscibility gap defined by the exsolved phases should be indicative of the temperature of exsolution if some constraints can be put on the composition of the ferromagnesian silicate in equilibrium with the chromite prior to its exsolution (Sack and Ghiorso 1991).

The minimum temperature of the exsolution can be constrained using the composition of homogenous Type I chromite from disseminated chromitite bodies from Los Guanacos, which has the lowest $Cr^{3+}/R^{3+}$ ratio (0.44–0.48; Table 2; Fig. 4). Temperature conditions equal to or higher than 600 °C are required to preserve this chromite as a homogenous phase, which is independent of the forsterite content of the olivine (Sack and Ghiorso 1991). Isothermal (isobaric) Cr-Al-$Fe^{3+}$ sections of the spinel prism at 600 °C (Sack and Ghiorso 1991) show that the slope of the empirical tie lines joining the pair of exsolutions of spinel-rich and magnetite-rich phases match with those calculated by Sack and Ghiorso (1991) when the equilibrium olivine composition is $Fo_{80}$ or $Fo_{95}$ (Figs. 4a and 4c). The first situation can apply to exsolved phases in chromite with very similar compositions reported from layered intrusions (Purvis et al. 1972; Muir and Naldrett 1973; Loferski and Lipin 1983; Eales et al. 1988; Zakrzewski 1989; Jan et al. 1992; van der Veen and Maaskant 1995; Appel et al. 2002; Garuti et al. 2003; Krause et al. 2007; Ahmed et al. 2008) but is at odds with the presumed setting of the ultramafic rocks from the Argentinian Central Andes (Proenza et al. 2008 and references therein). Therefore, we suggest that an olivine of ~$Fo_{95}$ was in equilibrium with the precursor chromite at around 600 °C in Los Guanacos (Fig. 4c). This interpretation is consistent with the fact that the relic clinopyroxene associated with Type I chromite is highly magnesian ($X_{Mg} = 0.954 \pm 0.004$) and presumably, cogenetic. Tamura and Arai (2004, 2005) reached a similar conclusion from the Iwanai-dake peridotite complex from Hokkaido (Japan), which in this case was supported by the preservation of magmatic olivine with $Fo_{92–95}$.

The estimated minimum temperature for the exsolution (ca. 600 °C) from Los Guanacos (and most likely also from Los Congos) matches with the thermal conditions of amphibolite-granulite facies metamorphism (590–730 °C) that is inferred to have affected the ultramafic bodies from the southern part of the Eastern Pampean Ranges of Córdoba (Rapela et al. 1998; Escayola et al. 2004; Martino et al. 2010). Under these conditions in the crust, the inferred minimum temperature for Los Guanacos and Los Congos precludes the coexistence of hydrous phases with chromite during the exsolution process (Gervilla et al. 2012).

**TABLE 4.** Oxide spinels, ideal composition, and selected structural data

| Mineral name | Cation | | Formulas | $x$[a] | $a$ (Å)[b] | $u$[c] |
|---|---|---|---|---|---|---|
| | A | B | | | | |
| **2-3 spinels ($A^{2+}B_2^{3+}O_4$)** | | | | | | |
| Hercynite | Fe | Al | $(Fe^{2+})[Al]_2O_4$[d] | N(0.00)[h] | 8.149 | 0.265 |
| Spinel | Mg | Al | $(Mg)[Al]_2O_4$ | N(0.01–0.07)[f,h] | 8.083 | 0.262 |
| | Co | Al | $(Co^{2+})[Al]_2O_4$ | N(0.15–0.20)[f,h] | 8.095 | 0.264 |
| | Cu | Al | $(Cu^{2+})[Al]_2O_4$ | N(0.40)[f,h] | 8.086 | na[j] |
| Galaxite | Mn | Al | $(Mn)[Al]_2O_4$ | N(0.30)[f,h] | 8.241 | 0.265 |
| Gahnite | Zn | Al | $(Zn)[Al]_2O_4$ | N(0.00–0.03)[f,h] | 8.086 | 0.264 |
| | Fe | Co | $(Co^{3+})[Fe^{2+}Co^{3+}]O_4$ | I(1.00)[f,h] | 8.254 | na |
| Chromite | Fe | Cr | $(Fe^{2+})[Cr]_2O_4$ | N(0.00)[h] | 8.392 | na |
| Magnesiochromite | Mg | Cr | $(Mg)[Cr]_2O_4$ | N(0.00)[h] | 8.333 | 0.261 |
| | Fe | Ga | $(Fe^{2+})[Ga]_2O_4$ | I(1.00)[f,h] | 8.360 | na |
| | Zn | Ga | $(Zn)[Ga]_2O_4$ | N(0.00)[f,h] | 8.330 | 0.262 |
| Magnetite | Fe | Fe | $(Fe^{3+})[Fe^{2+}Fe^{3+}]O_4$ | I(1.00)[h] | 8.394 | 0.255 |
| Magnesioferrite | Mg | Fe | $(Fe^{3+})[MgFe^{3+}]O_4$ | I(0.90)[h] | 8.360 | 0.257 |
| | Co | Fe | $(Co^{2+})[Fe^{3+}]_2O_4$ | I(1.00)[f,h] | 8.350 | 0.256 |
| Cuprospinel | Cu | Fe | $(Fe^{3+})[CuFe^{3+}]O_4$ | I(0.66–1.00)[f,h] | 8.369 | 0.255 |
| Jacobsite | Mn | Fe | $(Mn)[Fe^{3+}]_2O_4$ | N(0.10–0.15)[f,h] | 8.511 | 0.262 |
| Trevorite | Ni | Fe | $(Fe^{3+})[NiFe^{3+}]O_4$ | I(1.00)[f,h] | 8.325 | 0.257 |
| Coulsonite | Fe | V | $(Fe^{2+})[V^{3+}]_2O_4$ | N(0.00)[f,h] | 8.416 | 0.260 |
| Magnesiocoulsonite | Mg | V | $(Mg)[V^{3+}]_2O_4$ | N(0.00)[f,h] | 8.453 | 0.261 |
| **4-2 spinels ($A^{4+}B_2^{2+}O_4$)** | | | | | | |
| Ulvöspinel | Ti | Fe | $(Fe^{2+})[TiFe^{2+}]O_4$ | I(1.00)[e,f,g,h] | 8.530 | 0.265 |
| Qandilite | Ti | Mg | $(Mg)[TiMg]O_4$ | I(1.00)[f,g,h] | 8.445 | 0.265 |
| | V | Fe | $(Fe^{2+})[V^{4+}Fe^{2+}]O_4$ | I(1.00)[f,h] | 8.421 | na |
| | V | Mg | $(Mg)[V^{4+}Mg^{2+}]O_4$ | I(1.00)[h] | 8.384 | 0.261 |
| Brunogeierite | Ge | Fe | $(Ge)[Fe^{2+}]_2O_4$ | N(0.00)[f,h] | 8.411 | 0.250 |
| | Ge | Mg | $(Ge)[Mg]_2O_4$ | N(0.00)[f,h] | 8.250 | 0.251 |
| | Sn | Mg | $(Mg)[SnMg]O_4$ | I(1.00)[f,h] | 8.600 | 0.250 |

[a] Inversion parameter, where N ($x \leq 0.5$) and I ($x \geq 0.5$) denotes predominantly normal and inverse spinels, respectively. [b] Unit-cell parameter; data from Hill et al. (1979). [c] Oxygen fractional coordinate; data from Hill et al. (1979). [d] The parentheses and brackets are used to denote the tetrahedrally and octahedrally coordinated sites, respectively. [e] Forster and Hall (1965). [f] Muller and Roy (1974). [g] Lindsley (1976). [h] Hill et al. (1979). [i] Wechsler and Von Dreele (1989). [j] Not available (na).

### Crystal-chemistry constraints on the partition coefficients

The observed crystal-crystal partition coefficients points to the effect that the crystal-chemistry of the spinel-rich ($MgAl_2O_4$) and magnetite-rich phases ($Fe^{2+}Fe_2^{3+}O_4$) has on all investigated elements except Cu and Sn (Table 3). The elements most sensitive to crystal-chemistry could be Zn, Ga, Co, Ni, Ti, and Sc (Table 3). On the other hand, Mn is only slightly more compatible in the magnetite-rich phase (Table 3).

Oxide spinel minerals comprise a large group of end-members (e.g., Biagioni and Pasero 2014) with the general formula $AB_2O_4$ (some of them are included in Table 4). The letters A and B represent a range of elements with different valences, and the formulas are conventionally represented as $(A^{2+})[B^{3+}]_2O_4$ (2-3 spinels) and $(A^{4+})[B^{2+}]_2O_4$ (4-2 spinels), where tetrahedrally and octahedrally coordinated sites are represented with parentheses and brackets, respectively. In normal spinels the tetrahedrally coordinated sites are occupied by A, whereas the octahedrally coordinated sites are occupied exclusively by B. In inverse spinels the tetrahedrally coordinated sites are occupied by B cations, whereas the octahedrally coordinated sites are occupied by A and B cations: $(B^{3+})[A^{2+}B^{3+}]O_4$ for 2-3 spinels and $(B^{2+})[A^{4+}B^{2+}]O_4$ for 4-2 spinels. Cation distribution and degree of ordering in spinel-type structures have been investigated intensely in the past half-century (e.g., see Price et al. 1982 and references therein). Early models were based on crystal field stabilization energies (e.g., McClure 1957; Dunitz and Orgel 1957) but these were later superseded by calculations of electrostatic lattice energy that showed the important role of ionic radii (O'Neill and Navrotsky 1983), pseudopotential orbital radii (Price et al. 1982), or ionic potential (Bosi et al. 2012; Fregola et al. 2012) in influencing cation site preferences in spinel structures. Different cations and their arrangements in octahedrally and tetrahedrally coordinated sites result in changes of the unit-cell parameter, $a$, as well as, in the oxygen fractional coordinate, $u$-parameter (e.g., Lavina et al. 2002; Stevanović et al. 2010). The latter parameter describes the deviation of the ideal cubic close packed (CCP) array and the angular distortion of the octahedrally coordinated oxygen polyhedron from the ideal octahedron; and it has been successfully used to predict the normal or inverse nature of 2-3 and 4-2 spinel end-members (e.g., O'Neill and Navrotsky 1983; Stevanović et al. 2010).

It can be envisaged that the observed differences in element partitioning between the spinel-rich and the magnetite-rich phases (and therefore their relative solubility) is ultimately related to their contrasting crystal-chemistry (i.e., larger $a$ and lower $u$ for magnetite relative to spinel, Table 4). Some possible end-members that might be involved in the observed partitioning are shown in Table 4. Contrary to the expectation there is not to clear correlation between $u$ and $D_{\mathrm{i}}^{\mathrm{Spl/Mag}}$. For the end-member gahnite ($ZnAl_2O_4$) $a$ and $u$ are effectively similar to spinel (8.0860 vs. 8.0832 Å and 0.2636 vs. 0.2624, respectively) (Table 4); this similarity probably explains the enrichment of Zn in the spinel-rich phase relative to the magnetite-rich phase ($D_{\mathrm{Zn}}^{\mathrm{Spl/Mag}} = 5.48 \pm 0.63$; Table 3). Compared to spinel, the Ga end-member $ZnGa_2O_4$ has also similar $u$ (0.2617) but contrasting $a$ (8.3300 Å) (Table 4), however it is still more compatible with the spinel-rich phase ($D_{\mathrm{Ga}}^{\mathrm{Spl/Mag}} = 2.23 \pm 0.40$; Table 3), suggesting that $u$ rather than $a$ controls the partitioning. However, this inference does not apply to jacobsite ($MnFe_2O_4$) that is slightly more compatible with the magnetite-rich phase ($D_{\mathrm{Mn}}^{\mathrm{Spl/Mag}} = 0.81 \pm 0.15$; Table 3) despite having *u* (0.2615) similar to the Ga end-member (Table 4). The lack of correlation between *u* (and/or *a*) and $D_i^{Spl/Mag}$ is corroborated by the partition of Cu, which probably is controlled by cuprospinel ($CuFe_2O_4$). In this case, although *u* is similar to magnetite (0.2550 vs. 0.2548, Table 4) Cu is equally partitioned in both phases ($D_{Cu}^{Spl/Mag} = 1.11 \pm 0.57$; Table 3).

Compared to crystal-melt equilibrium where the ionic radii and the elasticity of the crystal lattice are key parameters controlling partitioning (e.g., Blundy and Wood 1994), the factors controlling crystal-crystal partitioning are less well constrained. An attempt to correlate ionic radii with $D_i^{Spl/Mag}$ shows only a very weak dependency (Fig. 5). Divalent cations with radius greater than 0.65 Å are partitioned in the magnetite-rich phase (Fig. 5a). The correlation for trivalent and tetravalent cations is even less clear (Figs. 5b and 5c). This is in part due to the degree of ordering (normal vs. inverse) of the spinel. In inverse and partially inverse spinels the same trivalent cation in 2-3 spinels (or divalent cations in 4-2 spinels) occupies two different sites, resulting in two apparent ionic radii. This even makes the definition of element partitioning based on bulk analyses ambiguous as by definition they do not distinguish between sites. Moreover, the variable valence states of certain elements (such as V, Ti, Mn, or Co) further complicates this picture. The complex interplay between crystal-chemistry and the partitioning of minor and trace elements suggests a relative dependence on cell parameters and ionic radii of these elements in spinel-type structures. Nevertheless, the ultimate influence of crystal-chemistry on the partitioning is not yet deciphered, due to the lack of detailed studies about the site preference and valence states of minor and trace elements in the spinel structures.

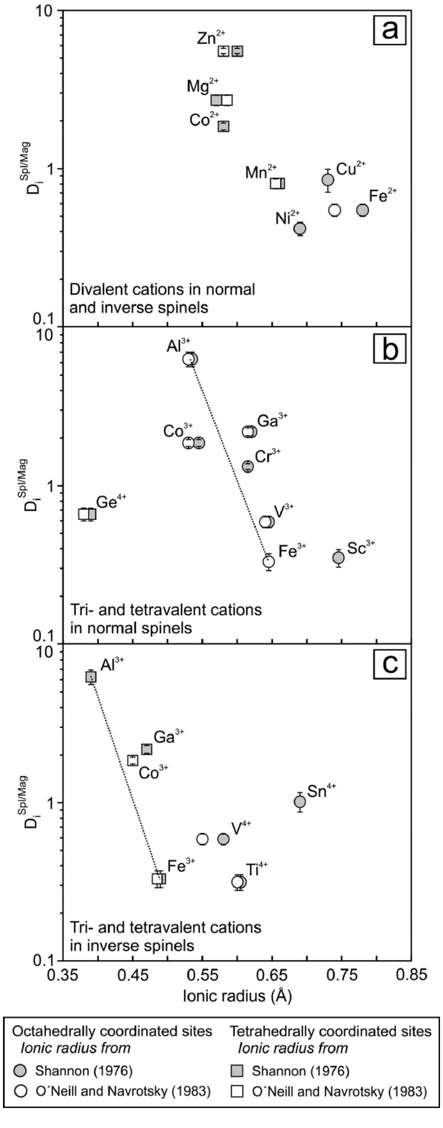

**FIGURE 5.** Plot of crystal-crystal partition coefficients vs. ionic radii (Shannon 1976; O'Neill and Navrotsky 1983) for divalent cations (**a**), trivalent and tetravalent cations in normal (**b**) and inverse spinels (**c**). Legend provided as inset in the figure.

## Comparison with chromite/melt element partitioning from high-temperature experiments

Since early experimental studies (e.g., Horn et al. 1994) it was noticed that the chromite/melt partitioning of certain minor and trace elements is a function of the composition of major elements in chromite. A direct comparison with our calculated $D^{Spl/Mag}$ is not always straightforward as the main exchange vectors experimentally investigated regarding trivalent cations are mostly limited to $Fe^{3+}Cr_{-1}$ (e.g., Horn et al. 1994) and $AlCr_{-1}$ (Wijbrans et al. 2015; these authors also presented data for two compositions along the vector $Fe^{3+}Al_{-1}$). The remarkable agreement of the partitioning data from the exsolved phases in chromite from this study and from the literature (Fig. 3), spanning all possible ranges of $Cr^{3+}/R^{3+}$ ratio of the solvus (from nearly zero to 0.6; Sack and Ghiorso 1991), suggest that the main factor controlling the partitioning in exsolved phases is not due to variations in $Cr^{3+}$ but due to the exchange vector $Fe^{3+}Al_{-1}$.

High-temperature (HT) partitioning experiments for Ti and Sc are consistent among several studies and indicate an increase in $D_{Ti}^{Spl/Mag}$ and $D_{Sc}^{Spl/Mag}$ with increasing $Fe^{3+}$ under otherwise constant pressure and temperature conditions but variable oxygen fugacity (Irving 1978; Horn et al. 1994; Nielsen et al. 1994; Nielsen and Beard 2000). This is consistent with the preference of Ti and Sc for the magnetite-rich phase observed in this study (Fig. 3); these elements are among the most sensitive to spinel crystal-chemistry ($D_{Ti}^{Spl/Mag} = 0.30 \pm 0.06$ and $D_{Sc}^{Spl/Mag} = 0.33 \pm 0.09$; Table 3). Recent experiments by Wijbrans et al. (2015) further support the preference of Ti and Sc for $Fe^{3+}$- and Cr-rich (Al-poor) spinels. These authors also observed only a small compositional effect on $D_{Mn}^{Spl/Mag}$ in $Fe^{3+}$-rich spinels, in line with our observations ($D_{Mn}^{Spl/Mag} = 0.81 \pm 0.15$; Table 3) and with the literature data ($D_{Mn}^{Spl/Mag} = 0.83 \pm 0.42$; Fig. 3). Ni is expected to be more compatible in magnetite (through the trevorite component, $NiFe_2O_4$, with inverse nature; Table 4) than in Al-rich spinels, as found in the present study ($D_{Ni}^{Spl/Mag} = 0.42 \pm 0.09$; Table 3) and in other exsolved phases in chromite from the literature ($D_{Ni}^{Spl/Mag} = 0.46 \pm 0.28$; Fig. 3). However, chromite/melt partitioning experiments performed by Righter et al. (2006) and Wijbrans et al. (2015), did not reveal any clear relationship between the partitioning of Ni in chromite and variations in major element components, except for the amount of Ni itself (Righter et al. 2006). Furthermore, the compositional effect on the partitioning of V cannot be inferred directly from experimental studies because it is strongly linked to the effects of temperature and oxygen fugacity (Horn et al. 1994; Nielsen et al. 1994; Canil 1999; Toplis and Corgne 2002; Lee et al. 2005; Righter et al. 2006; Mallmann and O'Neill 2009).

Contrary to our observations (Fig. 3; Table 3), the compositional effect on Ga, Co, and Zn partitioning in exsolved phases in chromite with contrasting major element compositions (Horn et al. 1994; Righter et al. 2006; Wijbrans et al. 2015) has not been reported so far. Wijbrans et al. (2015) reported some experimental challenges regarding these elements at high temperatures (>1300 °C) and low oxygen fugacity, explaining it due to the volatility of Zn and Ga and alloying of Co with the Pt wire. Another possible explanation is that these elements are only sensitive to $Fe^{3+}Al_{-1}$ variations, which have been poorly experimentally constrained. If so, partitioning data from the exsolved phases in chromite will represent a valuable source of information about the dependency of Ga, Co, and Zn partitioning on compositions along the $MgFe_{-1}$-$Al_2Fe^{3+}_{-2}$ exchange vector; this information could be extrapolated with caution to chromite/melt partitioning.

In summary it can be concluded that the results of HT experiments and low-temperature (LT) exsolutions in chromite are generally in agreement and suggest a significant dependence of Ti and Sc partitioning on $Fe^{3+}$ substitution in chromite. We speculate that, rather than temperature, the compositional effect on Ga, Co, and Zn observed exclusively in the exsolved phases from chromite is due to crystal-chemistry differences along the $MgFe_{-1}$-$Al_2Fe^{3+}_{-2}$ exchange vector (spinel-magnetite vector). The implications of this inference and some observations that might support it will be further explained below.

## IMPLICATIONS

The compositional effect that major elements has on minor and trace element partitioning in the exsolved phases in chromite, as deduced from this study, might give some insights into the origin of some compositional trends (or lack of trends) of chromite reported from different magmatic settings and those associated with metamorphism (Fig. 6; see Appendix for data sources).

The linear positive covariation shown by Co and Zn in chromite from magmatic suites is remarkable and suggests a constant relative solubility of Co and Zn (probably as $CoAl_2O_4$ and $ZnAl_2O_4$, gahnite, end-members in a 1:3 molar proportion; Fig. 6a). Moreover these elements are both correlated (particularly for layered intrusions) with the $MgAl_2O_4$ component in the chromite (Fig. 6a). The strong positive correlation is also noteworthy between Co and Ga in chromite from layered intrusions (probably suggesting a 6:1 molar mix of $CoAl_2O_4$ and $ZnGa_2O_4$), which is not observed in ophiolitic peridotites nor in lavas (Fig. 6b). Compared to other magmatic settings, major element compositional variations in chromite from layered intrusions correspond mostly to the exchange vectors $MgFe_{-1}$-$Al_2Fe^{3+}_{-2}$, with minor variations of Cr/(Cr+Al) atomic ratio (e.g., Barnes

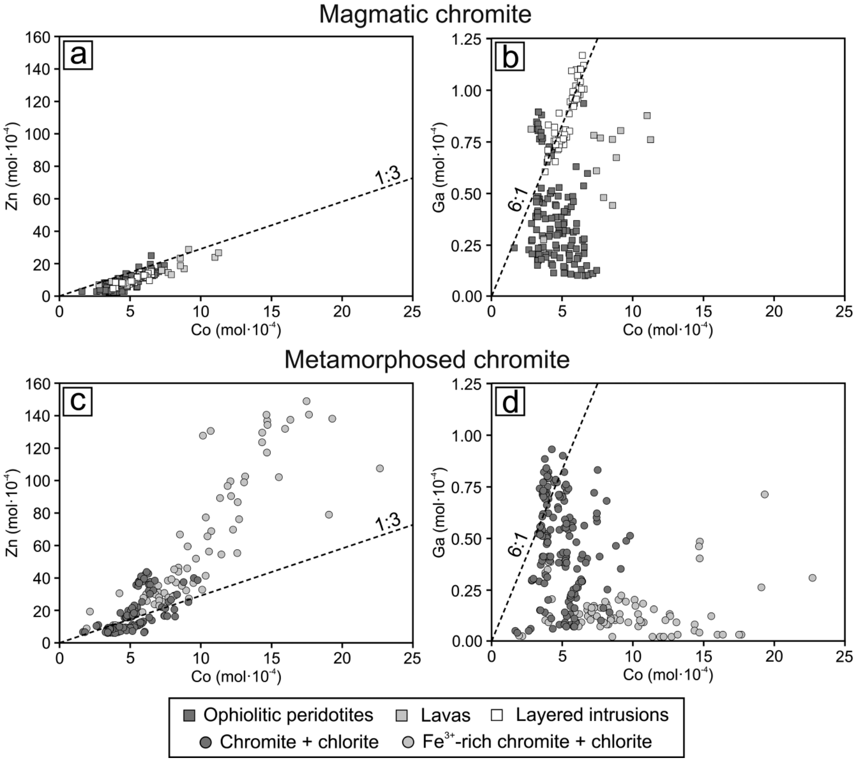

**FIGURE 6.** Compositional variation in terms of Co ($mol·10^{-4}$) vs. Zn ($mol·10^{-4}$) and Ga ($mol·10^{-4}$) in chromite from different magmatic settings (**a** and **b**), and affected by hydrous metamorphism (**c** and **d**). Legend provided as inset in the figure and data sources are listed in the Appendix.

and Roeder 2001). This further supports our previous suggestion that Zn, Co, and Ga partitioning is mostly sensitive to variations in $MgFe_{-1}$-$Al_2Fe^{3+}_{-2}$. As a whole, these trends probably reflect gradual compositional changes in chromite in equilibrium with melt (and/or olivine) in response to variations in temperature and/or composition.

Our observations have also some implications for our understanding of the disturbance of magmatic patterns in minor and trace elements during hydration and metamorphism of chromitite bodies. Chromite in apparent textural equilibrium with chlorite shows a distinctive departure from the magmatic trends discussed above (Figs. 6c and 6d). Chromite associated with chlorite, but particularly those enriched in $Fe^{3+}$ (i.e., $Fe^{3+}$-rich chromite), have considerably higher Co and Zn contents than magmatic chromite. Moreover the Co:Zn ratio is higher and more scattered in chlorite-bearing assemblages (Fig. 6c). This increase in Co and Zn is associated with a decrease in Ga particularly in $Fe^{3+}$-rich chromite (Fig. 6d). Whereas the decrease in Ga could be explained by an important change in the chromite composition, the coeval enrichment of Zn and Co is not consistent with the increase in the $Fe_3O_4$ component in the chromite, which is less variable related to hydrous metamorphism (Barnes 2000; Barnes and Roeder 2001; Mukherjee et al. 2010, 2015; Gervilla et al. 2012; Prabhakar and Bhattacharya 2013; Singh and Singh 2013; Gargiulo et al. 2013). The most likely explanation is that the contents of minor and trace elements in chromite affected by hydrous metamorphism are no longer controlled by the compositional changes of major elements in chromite but potentially to the chemistry of metamorphic fluids (e.g., fluids enriched in Zn and Co; Barnes 2000), which produce an incomplete reaction with magmatic chromite (i.e., presence of chromite cores) and the formation of hydrous phases in equilibrium with metamorphosed chromite (see Fig. 7 of Gervilla et al. 2012). Element partitioning between metamorphosed chromite and hydrous phases has not yet been thoroughly investigated. Interestingly, Colás (2015) reported chlorite from the metamorphosed chromitites of the Eastern Rhodope with relatively high contents of Ga (up to 30 ppm) and low contents of Zn and Co (below 15 and 18 ppm, respectively). Therefore, the formation of chlorite by interaction with fluids during hydrous metamorphism might explain the enrichment in Co and Zn coupled with strong depletion in Ga in chromite from metamorphosed chromitites of the Eastern Rhodope, as discussed by Colás et al. (2014).

## ACKNOWLEDGMENTS

This research was supported by the project CGL2010-15171 and F.P.I. grant BES-2011-045423 of the Ministerio de Econonía y Competitividad (Spain). Support for this study has also been provided by the FONDECYT #11140005 and "Millenium Nucleus for Metal Tracing Along Subduction NC130065" to José María González-Jiménez. We thank Steve Barnes and an anonymous reviewer for their careful and constructive comments and Ferdinando Bosi for his proficient editorial handling of this manuscript. The analytical data were obtained using instrumentation funded by DEST Systemic Infrastructure Grants, ARC LIEF, NCRIS, industry partners and Macquarie University. This is a contribution 701 from the ARC Centre of Excellence for Core to Crust Fluid Systems (www.ccfs.mq.edu.au) and 1055 in the GEMOC Key Centre (www.gemoc.mq.edu.au).

## REFERENCES CITED

Abzalov, M.Z. (1998) Chrome-spinels in gabbro-wehrlite intrusions of the Pechenga area, Kola Peninsula, Russia: Emphasis on alteration features. Lithos, 43, 109–134.

Ahmed, A.H., Helmy, H.M., Arai, S., and Yoshikawa, M. (2008) Magmatic unmixing in spinel from late Precambrian concentrically-zoned mafic-ultramafic intrusions, Eastern Desert, Egypt. Lithos, 104, 85–98.

Akmaz, R.M., Uysal, I., and Saka, S. (2014) Compositional variations of chromite and solid inclusions in ophiolitic chromitites from the southeastern Turkey: Implications for chromitite genesis. Ore Geology Reviews, 58, 208–224.

Appel, C., Appel, P., and Rollinson, H. (2002) Complex chromite textures reveal the history of an early Archaean layered ultramafic body in West Greenland. Mineralogical Magazine, 66, 1029–1041.

Bach, W., Paulick, H., Garrido, C.J., Ildefonse, B., Meurer, W.P., and Humphris, S.E. (2006) Unraveling the sequence of serpentinization reactions: Petrography, mineral chemistry, and petrophysics of serpentinites from MAR 15°N (ODP Leg 209, Site 1274). Geophysical Research Letters, 33, L13306.

Barnes, S.J. (1998) Chromite in komatiites, 1. Magmatic controls on crystallization and composition. Journal of Petrology, 39, 1689–1720.

——— (2000) Chromite in komatiites, II. Modification during greenschist to mid-amphibolite facies metamorphism. Journal of Petrology, 41, 387–409.

Barnes, S.J., and Roeder, P.L. (2001) The range of spinel compositions in terrestrial mafic and ultramafic rocks. Journal of Petrology, 42, 2279–2302.

Biagioni, C., and Pasero, M. (2014) The systematics of the spinel-type minerals: An overview. American Mineralogist, 99, 1254–1264.

Blundy, J., and Wood, B. (1994) Prediction of crystal melt partition coefficients from elastic moduli. Nature, 372, 452–454.

Bosi, F., Hålenius, U., D'Ippolito, V., and Andreozzi, G.B. (2012) Blue spinel crystals in the $MgAl_2O_4$-$CoAl_2O_4$ series: Part II. Cation ordering over short-range and long-range scales. American Mineralogist, 97, 1834–1840.

Burkhard, D.J.M. (1993) Accessory chromium spinels: Their coexistence and alteration in serpentinites. Geochimica et Cosmochimica Acta, 57, 1297–1306.

Candia, M.A.F., and Gaspar, J.C. (1997) Chromian spinels in metamorphosed ultramafic rocks from Mangabal I and II complexes, Goiás, Brazil. Mineralogy and Petrology, 60, 27–40.

Canil, D. (1999) Vanadium partitioning between orthopyroxene, spinel and silicate melt and the redox states of mantle source regions for primary magmas. Geochimica et Cosmochimica Acta, 63, 557–572.

——— (2002) Vanadium in peridotites, mantle redox and tectonic environments: Archean to present. Earth and Planetary Science Letters, 195, 75–90.

Colás, V (2015) Modelos de alteración de cromititas ofiolíticas durante el metamorfismo, 240 p. Ph.D. thesis, Univerisidad de Zaragoza, Spain.

Colás, V., Gonzalez-Jimenez, J.M., Griffin, W.L., Fanlo, I., Gervilla, F., O'Reilly, S.Y., Pearson, N.J., Kerestedjian, T., and Proenza, J.A. (2014) Fingerprints of metamorphism in chromite: New insights from minor and trace elements. Chemical Geology, 389, 137–152.

Connolly, H.C. Jr., and Burnett, D. (2003) On type B CAI formation: experimental constraints on $fO_2$ variations in spinel minor element partitioning and reequilibration effects. Geochimica et Cosmochimica Acta, 67, 4429–4434.

Cremer, V. (1969) Die Mischkristallbildung im System Chromit-Magnetit-Hercynit zwischen 1000 und 500°C. Jahrbuch für Mineralogie Abhandlungen, 111, 184–205.

Dare, S.A.S., Pearce, J.A., McDonald, I., and Styles, M.T. (2009) Tectonic discrimination of peridotites using $f_{O_2}$-Cr# and Ga–Ti–$Fe^{III}$ systematics in chrome-spinel. Chemical Geology, 261, 199–216.

Droop, G. (1987) A general equation for estimating $Fe^{3+}$ concentrations in ferromagnesian silicates and oxides from microprobe analyses, using stoichiometric criteria. Mineralogical Magazine, 51, 431–435.

Dunitz, J., and Orgel, L. (1957) Electronic properties of transition-metal oxides-I: Distortions from cubic symmetry. Journal of Physics and Chemistry of Solids, 3, 20–29.

Eales, H., Wilson, A., and Reynolds, I. (1988) Complex exsolved spinels in layered intrusions within an obducted ophiolite in the Natal-Namaqua mobile belt. Mineralium Deposita, 23, 150–157.

Escayola, M., Proenza, J.A., Schalamuk, A., and Cábana, C. (2004) La secuencia ofiolítica de la faja ultramáfica de Sierras Pampeanas de Córdoba, Argentina. In E. Pereira, R. Castroviejo and F. Ortiz, Eds., Complejos ofiolíticos en Iberoamérica: guías de prospección para metales preciosos, 133–155. Proyecto XIII.1-CYTED, Madrid-España

Evans, B.W., and Frost, B.R. (1975) Chrome-spinel in progressive metamorphism-a preliminary analysis. Geochimica et Cosmochimica Acta, 39, 959–972.

Forster, R., and Hall, E. (1965) A neutron and X-ray diffraction study of ulvöspinel, $Fe_2TiO_4$. Acta Crystallographica, 18, 857–862.

Fregola, R.A., Bosi, F., Skogby, S., and Hålenius, U. (2012) Cation ordering over short-range and long-range scales in the $MgAl_2O_4$-$CuAl_2O_4$ series. American Mineralogist, 97, 1821–1827.

Frost, B.R., and Beard, J.S. (2007) On silica activity and serpentinization. Journal of Petrology, 48, 1351–1368.

Gao, S., Liu, X., Yuan, H., Hattendorf, B., Günther, D., Chen, L., and Hu, S. (2002) Determination of forty two major and trace elements in USGS and NIST SRM glasses by laser ablation-inductively coupled plasma-mass spectrometry. Geostandards Newsletter, 26, 181–196.

Gargiulo, M., Bjerg, E., and Mogessie, A. (2013) Spinel group minerals in metamorphosed ultramafic rocks from Río de Las Tunas belt, Central Andes, Argentina. Geologica Acta, 11, 133–148.

Garuti, G., Pushkarev, E.V., Zaccarini, F., Cabella, R., and Anikina, E. (2003)

Chromite composition and platinum-group mineral assemblage in the Uktus Uralian-Alaskan-type complex (Central Urals, Russia). Mineralium Deposita, 38, 312–326.

Gervilla, F., Padrón-Navarta, J., Kerestedjian, T., Sergeeva, I., González-Jiménez, J., and Fanlo, I. (2012) Formation of ferrian chromite in podiform chromitites from the Golyamo Kamenyane serpentinite, Eastern Rhodopes, SE Bulgaria: a two-stage process. Contributions to Mineralogy and Petrology, 164, 643–657.

González-Jiménez, J.M., Augé, T., Gervilla, F., Bailly, L., Proenza, J.A., and Griffin, W.L. (2011) Mineralogy and geochemistry of platinum-rich chromitites from the mantle-crust transition zone at Ouen Island, New Caledonia ophiolite. Canadian Mineralogist, 49, 1549–1569.

González-Jiménez, J.M., Locmelis, M., Belousova, E., Griffin, W.L., Gervilla, F., Kerestedjian, T.N., O'Reilly, S.Y., Pearson, N.J., and Sergeeva, I. (2015) Genesis and tectonic implications of podiform chromitites in the metamorphosed ultramafic massif of Dobromirtsi (Bulgaria). Gondwana Research, 27, 555–574.

Griffin, W., Powell, W., Pearson, N., and O'Reilly, S. (2008) GLITTER: data reduction software for laser ablation ICP-MS. In P. Sylvester, Ed., Laser Ablation-ICP-MS in the Earth Sciences. Mineralogical Association of Canada Short Course Series, 40, 204–207.

Hill, R.J., Craig, J.R., and Gibbs, G. (1979) Systematics of the spinel structure type. Physics and Chemistry of Minerals, 4, 317–339.

Horn, I., Foley, S.F., Jackson, S.E,. and Jenner, G.A. (1994) Experimentally determined partitioning of high field strength-and selected transition elements between spinel and basaltic melt. Chemical Geology, 117, 193–218.

Irving, A.J. (1978) A review of experimental studies of crystal/liquid trace element partitioning. Geochimica et Cosmochimica Acta, 42, 743–770.

Jan, M., Khan, M., and Windley, B. (1992) Exsolution in Al-Cr-Fe$^{+3}$-rich spinels from the Chilas mafic-ultramafic complex, Pakistan. American Mineralogist, 77, 1074–1074.

Kamenetsky, V.S., Crawford, A.J., and Meffre, S. (2001) Factors controlling chemistry of magmatic spinel: an empirical study of associated olivine, Cr-spinel and melt inclusions from primitive rocks. Journal of Petrology, 42, 655–667.

Krause, J., Brügmann, G.E., and Pushkarev, E.V. (2007) Accessory and rock forming minerals monitoring the evolution of zoned mafic–ultramafic complexes in the Central Ural Mountains. Lithos, 95, 19–42.

Lavina, B., Salviulo, G., and Della Giusta, A. (2002) Cation distribution and structure modelling of spinel solid solutions. Physics and Chemistry of Minerals, 29, 10–18.

Lee, C.A., Brandon, A.D., and Norman, M. (2003) Vanadium in peridotites as a proxy for paleo-$f_{O_2}$ during partial melting: prospects, limitations, and implications. Geochimica et Cosmochimica Acta, 67, 3045–3064.

Lee, C.A., Leeman, W.P., Canil, D., and Li, Z.A. (2005) Similar V/Sc systematics in MORB and arc basalts: implications for the oxygen fugacities of their mantle source regions. Journal of Petrology, 46, 2313–2336.

Li, C., Ripley, E.M., Tao, Y., and Mathez, E.A. (2008) Cr-spinel/olivine and Cr-spinel/liquid nickel partition coefficients from natural samples. Geochimica et Cosmochimica Acta, 72, 1678–1684.

Lindsley, D.H. (1976) The crystal-chemistry and structure of oxide minerals as exemplified by the Fe-Ti oxides. Reviews in Mineralogy, 3, L1–L60.

Locmelis, M., Pearson, N.J., Barnes, S.J., and Fiorentini, M.L. (2011) Ruthenium in komatiitic chromite. Geochimica et Cosmochimica Acta, 75, 3645–3661.

Loferski, P.J., and Lipin, B.R. (1983) Exsolution in metamorphosed chromite from the Red Lodge district, Montana. American Mineralogist, 68, 777–789.

Mallmann, G., and O'Neill, H.St.C. (2009) The crystal/melt partitioning of V during mantle melting as a function of oxygen fugacity compared with some other elements (Al, P, Ca, Sc, Ti, Cr, Fe, Ga, Y, Zr and Nb). Journal of Petrology, 50, 1765–1794.

Martino, R.D., Guereschi, A.B., and Anzil, P.A. (2010) Metamorphic and tectonic evolution at 31° 36′ S across a deep crustal zone from the Sierra Chica of Córdoba, Sierras Pampeanas, Argentina. Journal of South American Earth Sciences, 30, 12–28.

McClure, D.S. (1957) The distribution of transition metal cations in spinels. Journal of Physics and Chemistry of Solids, 3, 311–317.

Mondal, S.K., Ripley, E.M., Li, C., and Frei, R. (2006) The genesis of Archaean chromitites from the Nuasahi and Sukinda massifs in the Singhbhum Craton, India. Precambrian Research, 148, 45–66.

Muan, A. (1975) Phase relations in chromium oxide-containing systems at elevated temperatures. Geochimica et Cosmochimica Acta, 39, 781–802.

Muller, O., and Roy, R. (1974) The Major Ternary Structural Families. Springer, Berlin.

Muir, J., and Naldrett, A. (1973) A natural occurrence of two-phase chromium-bearing spinels. Canadian Mineralogist, 11, 930–939.

Mukherjee, R., Mondal, S.K., Rosing, M.T., and Frei, R. (2010) Compositional variations in the Mesoarchean chromites of the Nuggihalli schist belt, Western Dharwar Craton (India): Potential parental melts and implications for tectonic setting. Contributions to Mineralogy and Petrology, 160, 865–885.

Mukherjee, R., Mondal, S.K., González-Jiménez, J.M., Griffin, W.L., Pearson, N.J., and O'Reilly, S.Y. (2015) Trace-element fingerprints of chromite, magnetite and sulfides from the 3.1 Ga ultramafic–mafic rocks of the Nuggihalli greenstone belt, Western Dharwar craton (India). Contributions to Mineralogy and Petrology, 169, 1–23.

Nielsen, R.L., and Beard, J.S. (2000) Magnetite–melt HFSE partitioning. Chemical Geology, 164, 21–34.

Nielsen, R.L., Forsythe, L.M., Gallahan, W.E., and Fisk, M.R. (1994) Major-and trace-element magnetite-melt equilibria. Chemical Geology, 117, 167–191.

Norman, M., Pearson, N., Sharma, A., and Griffin, W. (1996) Quantitative analysis of trace elements in geological materials by laser ablation ICPMS: Instrumental operating conditions and calibration values of NIST glasses. Geostandards Newsletter, 20, 247–261.

Norman, M., Griffin, W., Pearson, N., Garcia, M., and O'Reilly, S. (1998) Quantitative analysis of trace element abundances in glasses and minerals: a comparison of laser ablation inductively coupled plasma mass spectrometry, solution inductively coupled plasma mass spectrometry, proton microprobe and electron microprobe data. Journal of Analytical Atomic Spectrometry, 13, 477–482.

O'Neill, H.St.C., and Navrotsky, A. (1983) Simple spinels; crystallographic parameters, cation radii, lattice energies, and cation distribution. American Mineralogist, 68, 181–194.

Pagé, P., and Barnes, S.J. (2009) Using trace elements in chromites to constrain the origin of podiform chromitites in the Thetford Mines ophiolite, Québec, Canada. Economic Geology, 104, 997–1018.

Paktunc, A., and Cabri, L. (1995) A proton-and electron-microprobe study of gallium, nickel and zinc distribution in chromian spinel. Lithos, 35, 261–282.

Perinelli, C., Bosi, F., Andreozzi, G.B., Conte, A.M., and Armienti, P. (2014) Geothermometric study of Cr-rich spinels of peridotite mantle xenoliths from northern Victoria Land (Antarctica). American Mineralogist, 99, 839–846.

Prabhakar, N., and Bhattacharya, A. (2013) Origin of zoned spinel by coupled dissolution–precipitation and inter-crystalline diffusion: evidence from serpentinized wehrlite, Bangriposi, Eastern India. Contributions to Mineralogy and Petrology, 166, 1047–1066.

Price, G.D., Price, S.L., and Burdett, J.K. (1982) The factors influencing cation site-preferences in spinels a new mendelyevian approach. Physics and Chemistry of Minerals, 8, 69–76.

Proenza, J., Zaccarini, F., Escayola, M., Cábana, C., Schalamuk, A., and Garuti, G. (2008) Composition and textures of chromite and platinum-group minerals in chromitites of the western ophiolitic belt from Pampean Ranges of Córdoba, Argentina. Ore Geology Reviews, 33, 32–48.

Purvis, A., Nesbitt, R., and Hallberg, J. (1972) The geology of part of the Carr Boyd Rocks Complex and its associated nickel mineralization, Western Australia. Economic Geology, 67, 1093–1113.

Rapela, C., Pankhurst, R., Casquet, C., Baldo, E., Saavedra, J., Galindo, C., and Fanning, C. (1998) The Pampean Orogeny of the southern proto-Andes: Cambrian continental collision in the Sierras de Córdoba. Geological Society, London, Special Publications, 142, 181–217.

Rasband, W. (2007) WS 1997–2007 ImageJ. U.S. National Institutes of Health, Bethesda, Maryland.

Righter, K., Campbell, A., Humayun, M., and Hervig, R. (2004) Partitioning of Ru, Rh, Pd, Re, Ir, and Au between Cr-bearing spinel, olivine, pyroxene and silicate melts. Geochimica et Cosmochimica Acta, 68, 867–880.

Righter, K., Leeman, W., and Hervig, R. (2006) Partitioning of Ni, Co and V between spinel-structured oxides and silicate melts: Importance of spinel composition. Chemical Geology, 227, 1–25.

Sack, R.O., and Ghiorso, M.S. (1991) Chromian spinels as petrogenetic indicators: Thermodynamics and petrological applications. American Mineralogist, 76, 827–847.

Shannon, R.D. (1976) Revised effective ionic radii and systematic studies of interatomic distances in halides and chalcogenides. Acta Crystallographica, 32, 751–767.

Singh, A.K., and Singh, R.B. (2013) Genetic implications of Zn-and Mn-rich Cr-spinels in serpentinites of the Tidding Suture Zone, eastern Himalaya, NE India. Geological Journal, 48, 22–38.

Stevanović, V., d'Avezac, M., and Zunger, A. (2010) Simple point-ion electrostatic model explains the cation distribution in spinel oxides. Physical Review Letters, 105, 075501.

Tamura, A.N., and Arai, S. (2004) Inhomogeneous spinel in chromitite from the Iwanai-dake peridotite complex, Hokkaido, Japan: Variations of spinel unmixing texture and chemical composition. Science reports of Kanazawa University, 48, 9–29.

——— (2005) Exsolved spinel in chromitite from the Iwanai-dake peridotite complex, Hokkaido, Japan: A reaction between peridotite and highly oxidized magma in the mantle wedge. American Mineralogist, 90, 473–480.

Toplis, M.J., and Corgne, A. (2002) An experimental study of element partitioning between magnetite, clinopyroxene and iron-bearing silicate liquids with particular emphasis on vanadium. Contributions to Mineralogy and Petrology, 144, 22–37.

Turnock, A., and Eugster, H. (1962) Fe-Al oxides: Phase relationships below 1000°C. Journal of Petrology, 3, 533–565.

van der Veen, A., and Maaskant, P. (1995) Chromian spinel mineralogy of the Staré Ransko gabbro-peridotite, Czech Republic, and its implications for sulfide mineralization. Mineralium Deposita, 30, 397–407.

Wechsler, B.A., and Von Dreele, R. (1989) Structure refinements of $Mg_2TiO_4$, $MgTiO_3$ and $MgTi_2O_5$ by time-of-flight neutron powder diffraction. Acta Crystallographica, B45, 542–549.

Whitney, D.L., and Evans, B.W. (2010) Abbreviations for names of rock-forming minerals. American Mineralogist, 95, 185–187.

Wijbrans, C., Klemme, S., Berndt, J., and Vollmer, C. (2015) Experimental determination of trace element partition coefficients between spinel and silicate melt: the influence of chemical composition and oxygen fugacity. Contributions to Mineralogy and Petrology, 169, 1–33.

Yao, S. (1999) Chemical composition of chromites from ultramafic rocks: application to mineral exploration and petrogenesis, 174 p. Ph.D. thesis, Macquarie University, Sydney, Australia.

Zakrzewski, M.A. (1989) Chromian spinels from Kusa, Bergslagen, Sweden. American Mineralogist, 74, 448–455.

Zhou, M., Robinson, P.T., Su, B., Gao, J., Li, J., Yang, J., and Malpas, J. (2014) Compositions of chromite, associated minerals, and parental magmas of podiform chromite deposits: The role of slab contamination of asthenospheric melts in suprasubduction zone envrionments. Gondwana Research, 26, 262–283.

MANUSCRIPT RECEIVED OCTOBER 26, 2015
MANUSCRIPT ACCEPTED FEBRUARY 5, 2016
MANUSCRIPT HANDLED BY FERDINANDO BOSI

## APPENDIX

### Data sources for calculated crystal-crystal partition coefficients

The crystal-crystal partition coefficients of exsolved phases in chromite from previously published data sets were calculated using reported EMPA data for minor elements. Chromite with exsolution textures come from the layered complexes of Carr Boyd Rocks Complex (Western Australia, Purvis et al. 1972), Giant Nickel Mine (British Columbia, Muir and Naldrett 1973), Red Lodge district (Montana, U.S.A., Loferski and Lipin 1983), Kuså (Sweden, Zakrzewski 1989), Chilas (Pakistan, Jan et al. 1992), Isua Greenstone Belt (Greenland, Appel et al. 2002) and the Eastern Desert (Egypt, Ahmed et al. 2008); from the Uralian-Alaskan-type complexes of Staré Ransko (Czech Republic, van der Veen and Maaskant 1995), Uktus (Russia, Garuti et al. 2003) and the Central Ural Mountains (Krause et al. 2007); and from the peridotite complex of Iwanai-dake (Japan, Tamura and Arai 2005).

### Data source for minor and trace elements in chromite

The data sources for minor and trace elements in chromite used in this study consist of previously published and new data sets. Chromite samples are classified based on magmatic setting (ophiolitic peridotites, lavas, and layered intrusions) and by metamorphic assemblage (chromite and $Fe^{3+}$-rich chromite in equilibrium with chlorite).

Reported minor and trace element compositions of chromite in ophiolitic peridotites come from the Thetford Mine Ophiolite (Canada, Pagé and Barnes 2009), Ouen Island and Dyne (New Caledonia, González-Jiménez et al. 2011; Colás et al. 2014), Mercedita, Tres Amigos and Rupertina (Cuba, Colás et al. 2014; González-Jiménez et al. 2015), and Luobusa (Tibet, Zhou et al. 2014). Chromite samples of lavas are taken from the East Pacific Rise, Bonin Island (Japan), Thetford Mine Ophiolite (Canada) (Pagé and Barnes 2009), and Solomon Island (Yao 1999); and those of layered intrusions from the Bushveld Complex (South Africa) and the Great Dike (Zimbabwe) (Yao 1999). Data for the metamorphosed chromite come from ophiolitic chromitites of Los Congos and Los Guanacos (Argentina), Central and Eastern Rhodope (Bulgaria, González-Jiménez et al. 2015; Colás et al. 2014), Ouen Island (New Caledonia, González-Jiménez et al. 2011) and Southeastern Turkey (Akmaz et al. 2014); and those from the greenstone belt of Nuggihalli (India, Mukherjee et al. 2015).

### Matlab script to plot spinel prism in 3D

The following is a simple Matlab script to plot the spinel prism that reads an input csv file consisting in four columns (without headers) as follow $Cr/R^{3+}$, $Al/R^{3+}$, $Cr/R^{3+}$, and $X_{Mg}$ in mole proportions.

```
clear all
data = importdata(’CongosExs.csv’);
λ = data(:,1:3);
points_x = transpose(1-data(:,4));

% Cartesian components of the triangle vertices r1, r2, r3;
% ri = (yi, zi), i = 1:3
% r1 r2 r3
vertex = [0 1 0.5; % y
0 0 1]; % z

% transformation to cartesian coordinates
points_y = zeros(1,length(λ));
points_z = zeros(1,length(λ));

for i = 1:length(λ)
points_y(i) = λ(i,1)*vertex(1,1)...
+λ(i,2)*vertex(1,2)...
+λ(i,3)*vertex(1,3);
points_z(i) = λ(i,1)*vertex(2,1)...
+λ(i,2)*vertex(2,2)...
+λ(i,3)*vertex(2,3);
end

scatter3(points_x,points_y,points_z)
xlabel(‘x’), ylabel(‘y’), zlabel(‘z’),
xlim([0 1]), zlim([0 1])
text(-0.05,-0.15,0,[‘Pc’],‘FontSize’,14)
text(-0.05,1.15,-0.1,[‘Sp’],‘FontSize’,14)
text(1,-0.15,0,[‘Chr’],‘FontSize’,14)
text(0,0.5,1.1,[‘Mf’],‘FontSize’,14)
text(1,0.5,1.1,[‘Mt’],‘FontSize’,14)
text(1.15,1.25,-0.1,[‘Her’],‘FontSize’,14)
hold on

daspect([1.7 1 1.1753])

% Prism
plot3([0 0 0 0 1 1 1 1 1 0 0 1],...
[0 1 0.5 0 0 1 0.5 0 0.5 0.5 1 1],...
[0 0 1 0 0 0 1 0 1 1 0 0])
```